

RADAR SENSING FEATURING BICONICAL ANTENNA AND ENHANCED DELAY AND SUM ALGORITHM FOR EARLY STAGE BREAST CANCER DETECTION

Sew S. Tiang, Mohammed Sadoon, Tareq F. Zanoon, Mohd F. Ain, and Mohd Z. Abdullah*

School of Electrical and Electronic Engineering, Universiti Sains Malaysia, Engineering Campus, Penang 14300, Malaysia

Abstract—A biconical antenna has been developed for ultra-wideband sensing. A wide impedance bandwidth of around 115% at bandwidth 3.73–14 GHz is achieved which shows that the proposed antenna exhibits a fairly sensitive sensor for microwave medical imaging applications. The sensor and instrumentation is used together with an improved version of delay and sum image reconstruction algorithm on both fatty and glandular breast phantoms. The relatively new imaging set-up provides robust reconstruction of complex permittivity profiles especially in glandular phantoms, producing results that are well matched to the geometries and composition of the tissues. Respectively, the signal-to-clutter and the signal-to-mean ratios of the improved method are consistently higher than 5 dB and 10 dB, corresponding to an average increase in image fidelity of more than 140% compared to conventional radar focusing technique.

1. INTRODUCTION

Early work on microwave imaging for breast cancer detection was based on the assumption of a homogeneous breast structure with high dielectric contrast between malignant and normal tissues reaching a ratio of 5 : 1 [1,2]. However, more recent studies suggest that this contrast might be significantly less than previously thought, while exhibiting more complicated heterogeneity [3]. This problem, together with dispersive nature of biological tissues [4], presents a more challenging case such that the requirement of an antenna design must exhibit good performance in terms of size, impedance matching

Received 22 October 2012, Accepted 1 December 2012, Scheduled 7 December 2012

* Corresponding author: Mohd Zaid Abdullah (mza@usm.my).

and radiation pattern over the desired bandwidth. Hence, an optimal antenna design that maintains a high degree of control of the pulse shape throughout the overall transmission path is needed to attain the spatial resolution and penetration required for image reconstruction. Recently, the application of UWB imaging techniques for medical imaging has imposed limitations on the physical size of the antenna in use [5]. Various types of ultra-wideband (UWB) antenna were proposed to be part of the microwave imaging; typical examples include pyramidal horn [6], tapered slot [7], antipodal [5], stacked patch [8], dielectric resonator [9], and printed monopole [10]. However, existing designs in the antenna's literature lead to a large size and extra lumps loads as the trade-off for a wider impedance bandwidth, which results in low efficiencies and manufacturability. Thus, biconical antenna has been proven to be an ideal candidate since it is generally regarded as possessing a behavior that is well suited to UWB applications. In this paper, a biconical antenna array is proposed, designed for radar-based breast imaging. Like conventional tomographic measurements, an antenna array is considered in this study since this geometry allows data to be captured from multiple views, thus enabling image reconstruction be performed in 2-D or 3-D if measurements are taken from multiple planes.

Traditionally, there are two imaging approaches for reconstructing microwave images. They are (i) the tomographic based and (ii) radar-based reconstructions [11]. Compared to the tomographic approach, radar-based techniques are computationally simple and effective. However, they do not recover the dielectric profile, but rather display an image as a variance of energy intensity. The Delay and Sum (DAS) algorithm is one of the radar-based techniques first proposed for breast cancer detection in 1998 [12]. Over the years this algorithm has undergone several enhancements and iterative refinements [13]. An enhanced version of the delay and sum (EDAS) has been developed and tested in our lab, where the initial results obtained from simulated and experimental recordings demonstrate the capability of effectively reducing clutter and improving the image-to-signal ratio [14]. As compared to DAS, EDAS comprises two processing techniques, which are focusing quality and multiplication in pair. For the first method, weighted coherence factor (CF), also known as side lobe suppressing method, reduces the clutters of the backscattered signals by appropriately time-gating the arrival pulses [15]. Meanwhile, the multiplication in pair multiplies signals measured from the same transmitter in pair, effectively summing the radar impulses to create a synthetic focal point. An extra clutter reduction can theoretically be achieved by increasing the sample size as in the multistatic case [16]. As

a result, EDAS improves reconstruction as it acquires more information regarding the target. In this paper, the reconstructed images of DAS algorithm are compared with EDAS algorithm with respect to measurement uncertainties for homogeneous and heterogeneous breast phantoms. Also, two metrics are used to quantitatively assess the quality of the focusing algorithms. They are (i) signal-to-clutter-ratio (SCR) and (ii) signal-to-mean-ratio (SMR) [17, 18].

2. ANTENNA DESIGN

Biconical antenna is generally regarded as a high performance UWB antenna, which is suitable use for microwave imaging. The power transmitted is constant with respect to the azimuth but varies as a function of the elevation, cone heights, cone angles and frequency [19]. The cone height of a biconical antenna primarily influences the lower cut-off frequency, while the cone angle influences the input impedance. A biconical antenna with cone angle of 45° and cone height of 10 mm is considered in this study. The antenna is driven via a $50\ \Omega$ coaxial feeder which incorporates an in-line balun in the form of ferrite torroid through which the coaxial cable is threaded [20]. This arrangement ensures a balanced antenna feed and stable frequency response. In the fabrication, the coax centre conductor is connected to the apex of the lower cone, while the coax outer conductor is connected to the upper cone. The height of upper and lower cones, H_U and

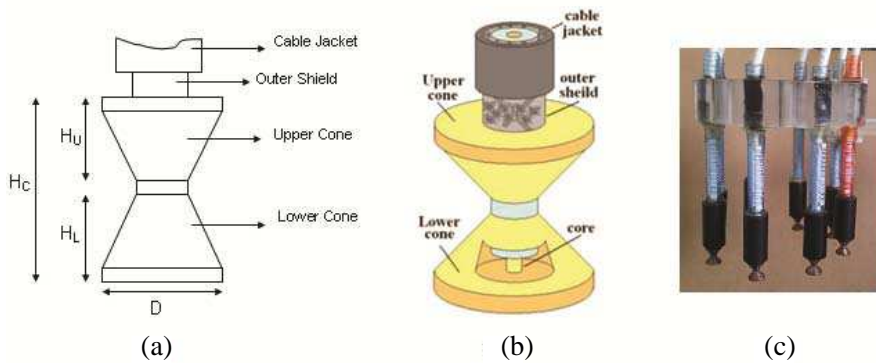


Figure 1. (a) Schematic of the biconical antenna. (b) Internal connection of coaxial cable with the biconical antenna. (c) An array of 8 equally distributed biconical antennas with coaxial cable connected with ferrite.

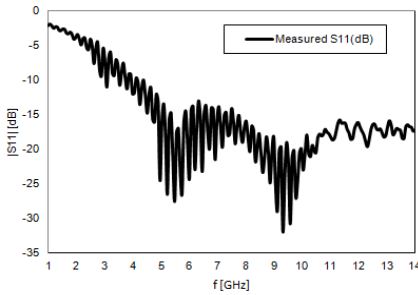


Figure 2. Measured reflection coefficient $|S_{11}|$ (dB) of biconical antenna.

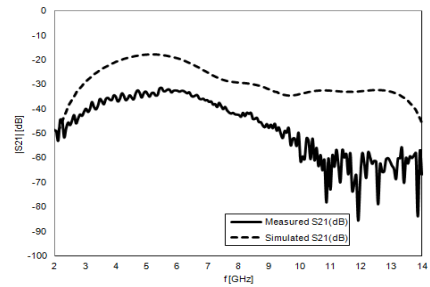


Figure 3. Simulated and measured transmission coefficient $|S_{21}|$ (dB) of biconical antenna.

H_L is 4 mm respectively. The total height of the whole biconical antenna, H_C is 10 mm [21]. A cylindrical globule of epoxy resin (Araldite) at the cone apex provides mechanical strength to the antenna. Figure 1(a) displays the schematic of the antenna design while Figure 1(b) shows the internal connection between the antenna and coaxial cable. Meanwhile Figure 1(c) shows the real antenna array with coaxial cable connected with ferrite torroid. Both antenna cones are machined from pure copper material, while an RG-58 coaxial is used to drive the antenna, achieving an impedance matching of $50\ \Omega$. For the purpose of achieving high detection resolutions and good clutter rejection, the antenna with an impedance bandwidth 4 to 10 GHz is typically employed [22]. Antenna measurements in free space are performed with an Agilent N5245A PNA-X Network Analyzer providing measurements up to 50 GHz. Figure 2 shows the measured reflection coefficient, S_{11} in free space. The bandwidth of the proposed antenna ranges from 3.73 to 14 GHz ($S_{11} < -10$ dB), with impedance matching greater than 115%. Hence, the frequency coverage of the proposed design is sufficiently wide and relatively stable for the desired bandwidth. During probing, two radar sensing elements are used; one sensor acts as a transmitter while the other acts as a receiver. For imaging purpose, the transmission coefficient (S_{21}) which represents the coupling between the two sensors are being measured. As S_{21} increases the coupling improves, yielding better transmission. Figure 3 shows the simulated and measured transmission coefficients of the biconical antenna. It can be observed that the magnitude of the simulated transmission coefficient is approximately -20 dB in the frequency range from 2 to 14 GHz, while the measured transmission coefficient is around -38 dB across the required frequency range. A

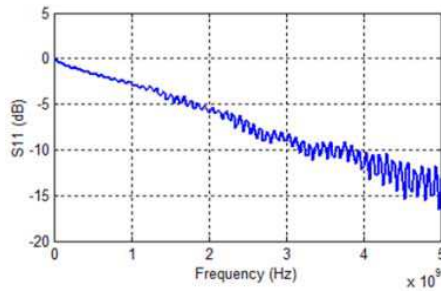


Figure 4. Measured reflection coefficient $|S_{11}|$ (dB) of biconical antenna in oil, for (0–5 GHz) frequency sweep.

maximum magnitude around 4.5 GHz is shown for both simulated and measured results. As suggested by earlier published studies, oil-based immersion liquid provides the best performance in terms of matching media and coupling material [23]. Figure 4 shows the measured reflection coefficient of the antenna taken in oil over the frequency range from 0 to 5 GHz. Examining Figure 4, the ripples are observed appearing at low frequencies due to poor impedance matching, while the UWB characteristic of the antenna with a return loss can be observed to steadily decrease as the frequency increases. The ideal case for reflection coefficient is at -10 dB at which only 10% of the power is reflected back to the source. Hence, the antenna bandwidth defined at -10 dB cut-off point is approximately 3 GHz. In addition to S_{11} and S_{21} , antenna pattern is also important in the antenna design as it shows the ability of the biconical antenna to focus energy into the breast rather than energy diverging out of the intended coverage area. Figure 5 shows the simulated radiation patterns of the antenna in oil for two different resonant frequencies (3.62 GHz and 9.63 GHz) in y - z plane. The resulting pattern appears like a figure “8” at low frequency, while the pattern becomes butterfly-shaped with the direction of the main beam being shifted at high frequency in the y - z plane. This trend is in agreement with other omnidirectional antennas as the biconical antenna also belongs to this category.

3. IMAGE RECONSTRUCTION

To validate the image reconstruction approach, both DAS and EDAS algorithms are tested using data obtained via numerical and experimental setups [14]. The results obtained are compared to assess the fidelity and accuracy of the proposed technique. As in the standard

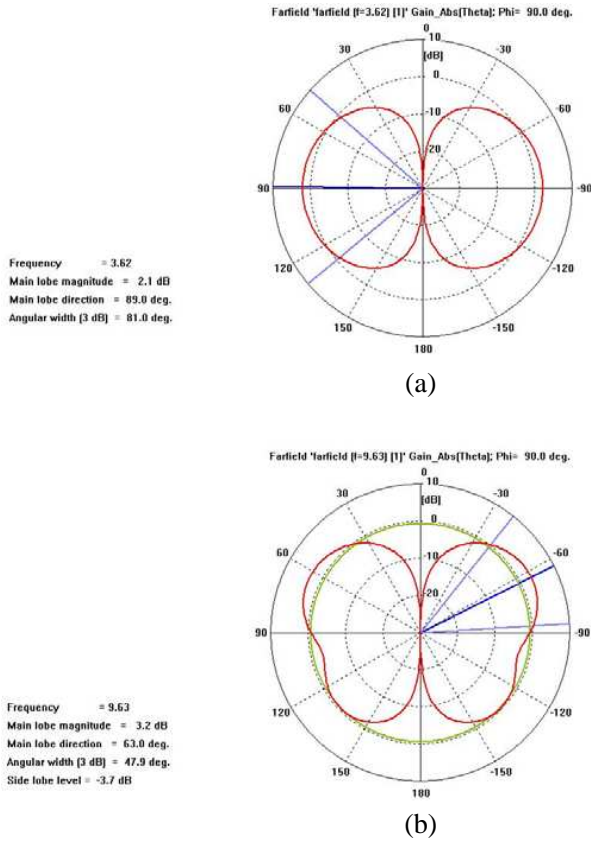


Figure 5. Simulated radiation patterns for biconical antenna at different frequencies in y - z plane. (a) 3.62 GHz. (b) 9.63 GHz.

DAS algorithm, the breast model is illuminated sequentially with a short ultra-wideband pulse from a number of sensors locations [16]. The distance from each transmitting sensor position to point of interest r and back to the receiving sensor position is calculated based on the average speed of propagation and the results are converted into time delays. Interested readers who wish to learn more about this technique are referred to earlier publications [16]. Unlike classical beam focussing techniques, the EDAS algorithm combines two processing techniques: focusing quality and multiplying in pair. In so doing, the round trip travelling time from each antenna to the focal point is firstly calculated, generating the backscattered signals with an appropriate time delay. This process is repeated until all focal points have been scanned and

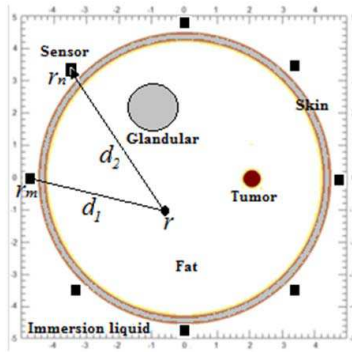


Figure 6. Region of interest illustrating distances d_1 and d_2 respectively from transmitter r_m to focal point r and back to receiver r_n .

the scattering energy corresponding to each focal point and for a given transmitted-received position has been calculated. Secondly, all these signals are summed up together and added coherently to produce a maximum energy at a given focal point. The energy is assigned to a pixel forming the profile of the scatterer. In order to obtain the tumor response, the calibration is firstly performed using standard subtraction procedure [24]. Effectively, this method removes the skin backscatters and other artefacts like the incident waves and clutters. Secondly, the backscattered signals resulting from the homogeneous model are subtracted channel-by-channel from signals obtained from cancerous model [17, 24].

Figure 6 shows the round trip distance from each sensor to the pixel of interest. The calculated value is converted into time samples based on the wave propagation speed. The delay time at each sensor (in unit of samples) can be calculated as follows:

$$\tau_{m,n}(r) = \frac{\|r_m - r\| + \|r_n - r\|}{v\Delta t} \quad (1)$$

where the velocity of propagation is given by $v = \frac{c}{\sqrt{\epsilon_r}}$, $\|r_m - r\|$ and $\|r_n - r\|$ are the distances between the focal point r and m th transmitter and n th receiver respectively. Δt is sample time, c is the velocity of light in vacuum and ϵ_r is the relative permittivity of the medium.

Following time alignment for each signal recorded at each focal point, a focusing-quality procedure is applied to remove the unwanted signals and noise artifacts [25]. This procedure is based on utilization of the coherence quality weighting of the backscattered signals at

specific focal point. Next, each signal pair measured from the same transmitter is multiplied with each other and their products summed. As this method acquires more information about the targets, extra clutter elimination is accomplished by increased sample size [16]. This procedure is similar to calculating the energy at each focal point. Mathematically:

$$E_n(r) = \int_0^w \left[\sum_{m=1}^M \sum_{n=1}^N y_{m,n}(t - \tau_{m,n}(r)) \right]^2 dt \quad (2)$$

where $y_{m,n}$ is the output signal after pairing multiplications and w the window length relative to the transmit pulse width. Each value is converted into a pixel and the assembly of this pixel forms an image.

To evaluate the performance for both algorithms, both the SCR and SMR ratios are used. Respectively, the calculations are as follow:

$$\text{SCR} = \frac{\max \text{ tumor energy}}{\max \text{ clutter energy}} \quad (3)$$

$$\text{SMR} = \frac{\max \text{ tumor energy}}{\text{mean energy}} \quad (4)$$

The SCR is given by ratio of the maximum tumor backscattered energy to the maximum clutter backscattered energy in the same image, while the SMR is given by ratio of the maximum tumor backscattered energy to the mean backscattered energy in the same image.

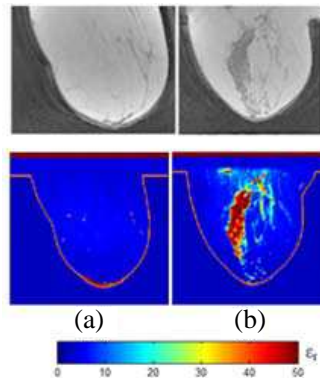


Figure 7. T1-MRI (upper) and their corresponding dielectric properties at 5 GHz (lower) of breast classification showing, (a) mostly fatty (< 25% glandular tissue), and (b) scattered fibro-glandular tissue (25–50% glandular).

4. MATERIALS AND METHODS

4.1. Homogeneous and Heterogeneous Phantoms

The breast is mainly composed of three types of tissues which are adipose, glandular, and connective tissue [26]. Recent studies on the dielectric properties of the breast suggest that the dielectric properties of normal breast tissue may vary depending on several factors [3], such as the tissue structure and amount of adipose. Consequently, the dielectric contrast between cancerous and normal tissues is reduced, leading to an increase of breast internal inhomogeneity. Figure 7 shows the composition of a homogeneous and a heterogeneous breast structure (< 50% glandular tissue) that has been derived from T1-weighted magnetic resonance images [3,27] and their corresponding anatomically derived dielectric properties. These numerical phantoms capture the structural heterogeneity of the breast tissue, incorporating the dispersive characteristics. The high permittivity values of the glandular structure can be clearly observed, where the variance of glandular and tumor properties is reduced. This situation is considered in the design of the test phantoms used in the experimentations.

4.2. Experimental Breast Phantom

To experiment the procedures on the varying breast structures [3], the homogeneous fatty and heterogeneous glandular models were constructed using chemical materials which are formulated based on the relative permittivity and conductivity of realistic tissue over the frequency of interest given in Table 1 [28]. In this research, an oil-in-gelatin mixture is used as a phantom material which is based on heterogeneous breast tissue dielectric properties presented in literature [29]. The phantom is similar to the one presented in [30] as all materials are dispersive with frequency-dependent characteristics similar to those presented in [29,31]. The breast phantom size is

Table 1. Relative permittivity and conductivity of breast tissues at frequency range from 200 MHz to 5 GHz.

Tissue	Relative Permittivity	Conductivity
Fat	11–18	0.1–0.2
Skin	33–46	0.15–3.8
Glandular	28–40	0.1–3.0
Tumor	48–66	0.15–5.0

fabricated simulating 76 mm diameter fatty tissue with 2 mm thick skin layer while the composition of the dense breast is more complex given the glandular structures that are heterogeneously distributed. In brief, the chemicals are mixed and molded into an 80 mm hemispherical shape, forming the breast phantom [29]. Meanwhile, the tumor with permittivity of 54 is molded into cylindrical shape rod with 5 mm diameter and inserted vertically inside the glandular area [28]. Figures 8(a) and 8(b) show the resulting homogenous and heterogeneously glandular breast phantoms.

4.3. Measurement and Data Acquisition System

The system configuration is composed of a set of 8 biconical antennas placed equidistantly around a circular shape phantom of 90 mm diameter forming full view geometry [19, 20]. Vegetable cooking oil is

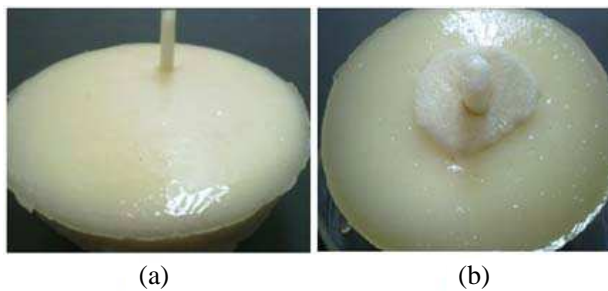


Figure 8. Experimental phantoms based on realistic T1-MRI images of an ordinary human breast, (a) homogeneous, and (b) heterogeneous models.

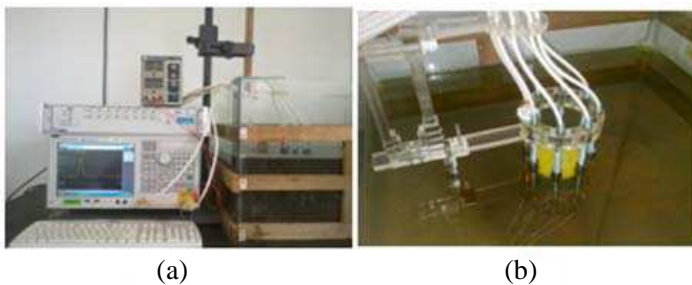


Figure 9. (a) The experimental set-up for UWB imaging. (b) Biconical antennas are placed equidistantly around the phantom.

used as the background immersion matching liquid in order to minimize interferences due to cluttering and multiple reflections. The wave speed in this medium is about 62% of the wave speed in air only. As the wave speed is slower, it offers better resolution in estimating the distances from each antenna to the breast surface [32]. In addition, oil can be assumed to be a lossless media due to its poor conductivity [33, 34]. The antennas are placed in a $60 \times 60 \times 50$ cm size glass tank filled with oil up to 35 cm in height and positioned at a constant height about 15 cm under the oil surface. In this way clutter caused by the reflections, particularly at the glass-tank and oil-air interfaces could be minimized by appropriately time gating the arrival pulses. The data acquisition system is composed of Cytec CXM 16 multiplexer that automatically switch transmitting and receiving lines, connected to an Agilent E5071C 8.5 GHz VNA, providing measurements in time domain. In addition, a wide band 20 dB amplifier is used to improve the received signal power. This acquisition system communicates with a high end workstation to automate data acquisition and process the reconstruction algorithms. Figures 9(a) and 9(b) show the actual experimental set up of the imaging system.

5. RESULTS AND DISCUSSION

5.1. Numerical Results

Figure 10(a) shows the cross section of the realistic MRI derived numerical homogeneous breast model using the Debye parameters [27]. Figures 10(b) and 10(c) show the images reconstructed using DAS and EDAS, respectively. Close examination of Figure 10(b) revealed the size and position of the target that have been accurately reconstructed,

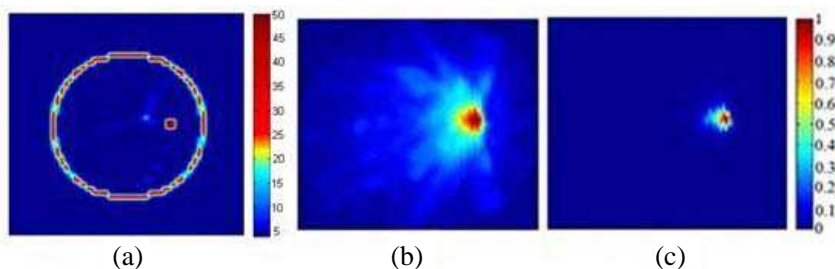


Figure 10. (a) Cross section of the T1-MRI derived numerical breast model, (b) numerical result of the model using DAS, and (c) numerical result of the model using EDAS.

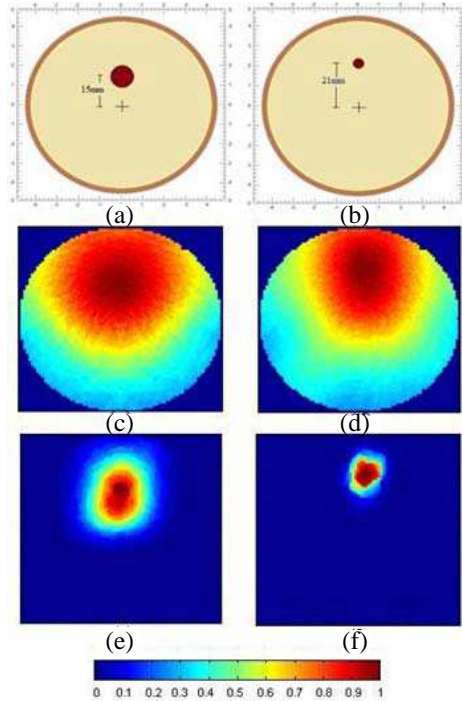


Figure 11. Experimental results of homogeneous breast phantom, (a) actual image with 10 mm tumor, (b) actual image with 5 mm tumor, (c) reconstructed image of (a) using DAS, (d) reconstructed image of (b) using DAS, (e) reconstructed image of (a) using EDAS, (f) reconstructed image of (b) using EDAS.

despite the present of some clutters in the image. As evident in Figure 10(c), a significant improvement in the reconstruction and image quality is observed by the reduction of almost all of the cluttering artifacts.

5.2. Experimental Results

Image reconstruction using real measurements are more challenging due to the noise associated with the experimental environment. Both homogeneous and the heterogeneous breast phantoms described previously are used in the experiments. Two homogeneous phantoms simulating 10 mm and 5 mm tumors are used in the homogeneous breast tests. The tumors are positioned at 15 mm and 21 mm away from the centre, embedded in the fatty tissue, as shown in Figures 11(a)

and 11(b) respectively. Figures 11(c) and 11(d) show the images reconstructed using DAS. Again it can be observed that these results contain artifacts and clutters, causing image blurring. Meanwhile, Figures 11(e) and 11(f) show images reconstructed using EDAS. It can be seen that the reconstructions are more accurate and the blurring is

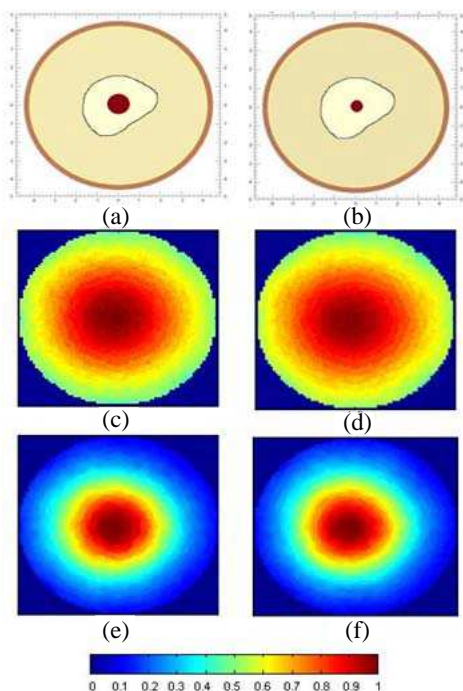


Figure 12. Experimental results of heterogeneous breast phantom, (a) actual image with 10 mm tumor, (b) actual image with 5 mm tumor, (c) reconstructed image of (a) using DAS, (d) reconstructed image of (b) using DAS, (e) reconstructed image of (a) using EDAS, (f) reconstructed image of (b) using EDAS.

Table 2. Comparison of SCR and SMR for DAS and EDAS algorithms in homogeneous model.

Model	Algorithm	Metric (dB)	10 (mm)	5 (mm)
Homogeneous	DAS	SCR	3.11	4.2
		SMR	6.1	6.32
	EDAS	SCR	7.93	9.11
		SMR	16.28	17.72

Table 3. Comparison of SCR and SMR for DAS and EDAS algorithms in heterogeneous model.

Model	Algorithm	Metric (dB)	10 (mm)	5 (mm)
Heterogeneous	DAS	SCR	2.01	3.18
		SMR	4.09	4.55
	EDAS	SCR	4.3	4.41
		SMR	11.32	11.51

visually less compared to standard EDAS technique. Table 2 shows the comparison of SCR and SMR for DAS and EDAS algorithms in homogeneous model, while Table 3 summarizes the results for heterogeneous model. Referring to 5 mm tumor, the EDAS resulted in SCR 9.11 dB and SMR 17.72 dB compared to DAS with SCR 4.2 dB and SMR 6.32 dB, respectively. Clearly, the clutter artifacts have successfully been removed in these reconstructions. Similar experimentations are performed on the heterogeneous phantom, where 10 mm and 5 mm tumors are embedded inside the glandular structure. In this case the dielectric contrast between tumor and bordering glandular tissue is approximately 1.7 : 1, simulating a typical ratio of an ordinary glandular type of an adult female breast [28]. The actual images corresponding to 10 mm and 5 mm tumors are shown in Figures 12(a) and 12(b), respectively. Figures 12(c) and 12(d) are images reconstructed using DAS, while Figures 12(e) and 12(f) are the reconstructed images obtained using EDAS. Again, the EDAS has produced a much better reconstruction for 5 mm tumor in heterogeneous model compared to DAS, resulting in an improved SCR and SMR of 42% and 57%, respectively. In spite of a low contrast ratio, the EDAS is still able to accurately map the heterogeneous structures including the localization of the tumor. Nevertheless, only a slight difference in term of the target size is observed from the results. This shortcoming can be attributed to the linear nature of radar based methods in solving the nonlinear inverse scattering problem. As observed from Tables 2 and 3, the SCR and SMR ratios for both algorithms decreased significantly with increasing dielectric heterogeneity of tissues, thus reducing the localization performance.

6. CONCLUSION

In this paper, biconical antenna has been demonstrated to provide a good reflection coefficient covering UWB impedance bandwidth, which constitutes an important feature in imaging application. The

antenna array provides more processing gain for UWB applications, increasing the gathered information as well as reducing the clutter in the measurements. These antennas are used together with the homogeneous and heterogeneous breast phantoms and oriented for early detection of cancerous tissue. Image reconstructions are performed using the proposed EDAS method and results are compared with the original DAS algorithm. Experimental results indicated that both algorithms have successfully mapped the complex permittivity distribution inside the test phantoms, with EDAS producing a much better signal-to-noise ratio compared to DAS. Overall the EDAS has resulted in the improvement of SCR and SMR by 49% and 62%, respectively. The promising results of our laboratory experiments strongly encouraged us to implement the clinical prototype of the system. Preliminary results of the clinical trials will be presented in our future work. Also, future research will systematically focus in evaluating EDAS using planar type UWB sensors and results will be published in our future papers.

ACKNOWLEDGMENT

This project was supported by USM's Fundamental Research Grants 811063 and 6071222.

REFERENCES

1. Surowiec, A. J., S. S. Stuchly, J. R. Barr, and A. Swarup, "Dielectric properties of breast carcinoma and the surrounding tissues," *IEEE Transactions on Biomedical Engineering*, Vol. 35, No. 4, 257–263, 1988.
2. Joines, W. T., Y. Zhang, C. Li, and R. L. Jirtle, "The measured electrical properties of normal and malignant human tissues from 50 to 900 MHz," *Medical Physics*, Vol. 21, 547–550, 1994.
3. Lazebnik, M., D. Popovic, L. McCartney, C. B. Watkins, M. J. Lindstrom, J. Harter, S. Sewall, T. Ogilvie, A. Magliocco, and T. M. Breslin, "A large-scale study of the ultrawideband microwave dielectric properties of normal, benign and malignant breast tissues obtained from cancer surgeries," *Physics in Medicine and Biology*, Vol. 52, 6093–6115, 2007.
4. Xiao, X. and T. Kikkawa, "Early breast cancer detection by ultrawide band imaging with dispersion consideration," *Japanese Journal of Applied Physics*, Vol. 47, 3209–3213, 2008.
5. Chen, X., J. Liang, S. Wang, Z. Wang, and C. Parini, "Small

- ultra wideband antennas for medical imaging,” *2008 Loughborough Antennas & Propagation Conference*, 28–31, Loughborough, UK, 2008.
6. Li, X., E. J. Bond, B. D. Van Veen, and S. C. Hagness, “An overview of ultra-wideband microwave imaging via space-time beamforming for early-stage breast-cancer detection,” *IEEE Antennas and Propagation Magazine*, Vol. 47, No. 1, 19–34, 2005.
 7. Khor, W. C., M. E. Bialkowski, A. Abbosh, N. Seman, and S. Crozier, “An ultra wideband microwave imaging system for breast cancer detection,” *IEICE Transactions on Communications*, Vol. 90, No. 9, 2376–2381, 2007.
 8. Klemm, M., I. J. Craddock, J. A. Leendertz, A. Preece, and R. Benjamin, “Radar-based breast cancer detection using a hemispherical antenna array — Experimental results,” *IEEE Transactions on Antennas and Propagation*, Vol. 57, No. 6, 1692–1704, 2009.
 9. Huang, W. and A. Kishk, “Compact dielectric resonator antenna for microwave breast cancer detection,” *IET Microwaves, Antennas & Propagation*, Vol. 3, No. 4, 638–644, 2009.
 10. Golezani, J. J., M. Abbak, and I. Akduman, “Modified directional wide band printed monopole antenna for use in radar and microwave imaging applications,” *Progress In Electromagnetics Research Letters*, Vol. 33, 119–129, 2012.
 11. Fear, E. C., P. M. Meaney, and M. A. Stuchly, “Microwaves for breast cancer detection?,” *IEEE Potentials*, Vol. 22, No. 1, 12–18, 2003.
 12. Hagness, S. C., A. Taflove, and J. E. Bridges, “Two-dimensional FDTD analysis of a pulsed microwave confocal system for breast cancer detection: Fixed-focus and antenna-array sensors,” *IEEE Transactions on Biomedical Engineering*, Vol. 45, No. 12, 1470–1479, 1998.
 13. Byrne, D., M. O’Halloran, M. Glavin, and E. Jones, “Data independent radar beamforming algorithms for breast cancer detection,” *Progress In Electromagnetics Research*, Vol. 107, 331–348, 2010.
 14. Zanoon, T. F., M. S. Hathal, and M. Z. Abdullah, “Comparing image reconstruction algorithms for microwave camera featuring ultra wideband sensor,” *IEEE International Conference on Imaging System and Techniques*, 112–117, Penang, Malaysia, 2011.
 15. Hollman, K., K. Rigby, and M. O’Donnell, “Coherence factor of speckle from a multi-row probe,” *1999 IEEE Proceedings*

- Ultrasonics Symposium*, 1257–1260, Caesars, Tahoe, NV, 1999.
16. Nilavalan, R., A. Gbedemah, I. Craddock, X. Li, and S. C. Hagness, “Numerical investigation of breast tumour detection using multi-static radar,” *Electronics Letters*, Vol. 39, 1787–1789, 2003.
 17. Lim, H. B., N. T. T. Nhung, E. P. Li, and N. D. Thang, “Confocal microwave imaging for breast cancer detection: Delay-multiply-and-sum image reconstruction algorithm,” *IEEE Transactions on Biomedical Engineering*, Vol. 55, No. 6, 1697–1704, 2008.
 18. Conceicao, R. C., M. O’Halloran, M. Glavin, and E. Jones, “Comparison of planar and circular antenna configurations for breast cancer detection using microwave imaging,” *Progress In Electromagnetics Research*, Vol. 99, 1–20, 2009.
 19. Armitage, D. W., W. Yin, M. Z. Abdullah, M. Billal, and A. J. Peyton, “Antenna design for ultra wide band electromagnetic tomography,” *Proceedings of the 5th World Congress on Industrial Process Tomography*, Norway, UK, 2007.
 20. Zanoon, T. F., S. Binajja, and M. Abdullah, “Electromagnetic tomography featuring ultra wide band sensor with conformal finite difference (CFDTD) modeling of dispersive media,” *IEEE Symposium on Industrial Electronics & Applications*, 377–382, Kuala Lumpur, Malaysia, 2009.
 21. Samaddar, S. N. and E. L. Mokole, “Biconical antennas with unequal cone angles,” *IEEE Transactions on Antennas and Propagation*, Vol. 46, No. 2, 181–193, 1998.
 22. Valderas, D., J. I. Sancho, D. Puente, C. Ling, and X. Chen, *Ultrawideband Antennas: Design and Applications*, 174, 1st Edition, Imperial College Press, 2011.
 23. Sill, J. and E. Fear, “Tissue sensing adaptive radar for breast cancer detection: Study of immersion liquids,” *Electronics Letters*, Vol. 41, No. 3, 113–115, 2005.
 24. Shao, W., B. Zhou, Z. Zheng, and G. Wang, “UWB microwave imaging for breast tumor detection in inhomogeneous tissue,” *27th Annual International Conference of the IEEE Engineering in Medicine and Biology Society*, 1496–1499, Shanghai, China, 2006.
 25. Wang, S. L., C. H. Chang, H. C. Yang, Y. H. Chou, and P. C. Li, “Performance evaluation of coherence-based adaptive imaging using clinical breast data,” *IEEE Transactions on Ultrasonics, Ferroelectrics and Frequency Control*, Vol. 54, No. 8, 1669–1679, 2007.
 26. Conceicao, R. C., M. O’Halloran, M. Glavin, and E. Joines,

- “Numerical modeling for ultra wideband radar breast cancer detection and classification,” *Progress In Electromagnetics Research B*, Vol. 34, 145–171, 2011.
27. Zastrow, E., S. K. Davis, M. Lazebnik, F. Kelcz, B. D. Van Veen, and S. C. Hagness, “Development of anatomically realistic numerical breast phantoms with accurate dielectric properties for modeling microwave interactions with the human breast,” *IEEE Transactions on Biomedical Engineering*, Vol. 55, No. 12, 2792–2800, 2008.
 28. Porter, E., J. Fakhoury, R. Oprisor, M. Coates, and M. Popovic, “Improved tissue phantoms for experimental validation of microwave breast cancer detection,” *2010 Proceedings of the Fourth European Conference on Antennas and Propagation*, 1–5, Barcelona, Spain, 2010.
 29. Lazebnik, M., E. L. Madsen, G. R. Frank, and S. C. Hagness, “Tissue-mimicking phantom materials for narrowband and ultrawideband microwave applications,” *Physics in Medicine and Biology*, Vol. 50, 4245–4258, 2005.
 30. Hahn, C. and S. Noghianian, “Heterogeneous breast phantom development for microwave imaging using regression models,” *International Journal of Biomedical Imaging*, Vol. 2012, 1–12, 2012.
 31. Lazebnik, M., L. McCartney, D. Popovic, C. B. Watkins, M. J. Lindstrom, J. Harter, S. Sewall, A. Magliocco, J. H. Booske, M. Okoniewski, and S. C. Hagness, “A large-scale study of ultrawideband microwave dielectric properties of normal breast tissue obtained from reduction surgeries,” *Physics in Medicine and Biology*, Vol. 52, 2637–2656, 2007.
 32. Winters, D. W., J. D. Shea, E. L. Madsen, G. R. Frank, B. D. Van Veen, and S. C. Hagness, “Estimating the breast surface using UWB microwave monostatic backscatter measurements,” *IEEE Transactions on Biomedical Engineering*, Vol. 55, No. 1, 247–256, 2008.
 33. Zanoon, T. and M. Abdullah, “Early stage breast cancer detection by means of time-domain ultra-wide band sensing,” *Measurement Science and Technology*, Vol. 22, 114016, 2011.
 34. Cataldo, A., E. PiuZZi, G. Cannazza, E. De Benedetto, and L. Tarricone, “On the use of dielectric spectroscopy for quality control of vegetable oils,” *Proceedings of the XIX IMEKO World Congress Fundamental and Applied Metrology*, 433–437, Lisbon, Portugal, 2009.